Chemical Science

ROYAL SOCIETY OF CHEMISTRY

EDGE ARTICLE

View Article Online
View Journal | View Issue

Cite this: *Chem. Sci.*, 2025, **16**, 22757

All publication charges for this article have been paid for by the Royal Society of Chemistry

Effect of metal substitution on the intrinsic activity of iridium-based oxides for the oxygen evolution reaction

Yinghao Xu,†[a] Yi-Hsuan Wu,†[a] Paula M. Abdala,[a] Connor Sherwin,[b] Veronica Celorrio,[b] Diana Piankova,[a] Payal Chaudhary,[c] Vitaly Alexandrov,[cd] Agnieszka Kierzkowska,[a] Denis A. Kuznetsov *[a] and Christoph R. Müller *[a]

Iridium-based oxides are among the most promising catalysts for the acidic oxygen evolution reaction (OER) owing to their high catalytic activity and stability. Substituting iridium with earth-abundant elements could lower costs and potentially boost its intrinsic activity even further; however, no unambiguous structure–activity relationships describing the physical origins of the effect of the substituent for this class of electrocatalysts have been established. In this work, we utilized a series of IrO_x(:M) nanoparticle catalysts to correlate their *in situ* structural changes with intrinsic OER activity. We observe that IrO_x(:M) with M = W and In feature a significantly higher Ir-mass-normalized OER activity than IrO_x, however the activity enhancements have a different origin. While the increased activity of IrO_x : In stems from a higher number of electrochemically active iridium centers (due to the leaching of indium), IrO_x : W features a higher intrinsic OER activity compared to IrO_x, due to electronic effects of W on neighboring Ir/O sites. Furthermore, *operando* electrochemical mass spectrometry experiments and density functional theory (DFT) calculations revealed that the enhanced OER activity of IrO_x(:M) does not originate from a promotion of the lattice oxygen coupling mechanism, but is instead associated with a facilitated conventional adsorbate evolution mechanism.

Received 15th August 2025
Accepted 27th October 2025

DOI: 10.1039/d5sc06242j

rsc.li/chemical-science

Introduction

Iridium oxide is a benchmark anode electrocatalyst in proton-exchange membrane water electrolyzers (PEMWEs) owing to its high catalytic activity and electrochemical stability,[1–10] outperforming other catalyst materials including ruthenium oxide.[11,12] However, the scarcity of iridium is a considerable issue preventing the large scale implementation of PEMWEs.[13] The use of Ir-based mixed metal oxides in which Ir is partially substituted by another metal is a commonly employed strategy to reduce the precious metal content.[14–19] In addition, the partial substitution of Ir might provide an avenue to enhance the intrinsic activity of the Ir sites.

However, the instability of many Ir-containing complex oxides under OER conditions is a considerable challenge.[15,20–22] For example, although Ir-containing oxides, such as $SrIrO_3$ or La_2LiIrO_6, have a high surface-area-normalized OER activity,[20,21] they have also exhibited an appreciable degree of reconstruction resulting in the exsolution of $IrO_y(OH)_z \cdot nH_2O$ (also referred to as IrO_x) or crystalline IrO_2 on their surface.[23–29] Such complex transformations under OER conditions often lead to ill-defined, defective motifs that complicate an accurate description of the electronic and geometric structure of the active site (*i.e.*, the oxidation state and coordination number of iridium, Ir–O/OH bond length, *etc.*). Owing to this inherent complexity and structural dynamics of Ir-based systems, there has been a large number of studies aiming to explore the origins of their high OER activity and to formulate structure–activity correlations with the overarching goal to provide the tool to guide the design of highly active and stable, Ir-based (mixed) oxide electrocatalysts.[15,20,23–25,30–32] It was found that the structure of IrO_x under OER conditions is strongly influenced by the precursor composition, however the relationship between the precursor structure and the resulting catalyst phase remains poorly understood.[17,21,27,33]

A key challenge in understanding the impact of dopants/substituents on the structure and OER activity of Ir-based catalysts is that most studies report electrode surface area- or mass-normalized OER activities without accounting for the fraction of catalytically- or redox-active IrO_x sites. Further,

[a]*ETH Zürich, Department of Mechanical and Process Engineering, 8092 Zürich, Switzerland. E-mail: denisk@ethz.ch; muelchri@ethz.ch*

[b]*Diamond Light Source, Harwell Science and Innovation Campus, Didcot, OX11 0DE, UK*

[c]*Department of Chemical and Biomolecular Engineering, University of Nebraska-Lincoln, Lincoln, Nebraska 68588, USA*

[d]*Nebraska Center for Materials and Nanoscience, University of Nebraska-Lincoln, Lincoln, Nebraska 68588, USA*

† These authors contribute equally.

improvements in the catalytic activity of Ir-based catalysts have frequently been attributed, often without unequivocal experimental evidence, to electronic modulation of iridium by the substituent M. Indeed, in many cases, only the structure of the precursor materials was assessed, *i.e.*, the structures that may not exist under actual reaction conditions, as the true active state of the catalysts could be a monometallic IrO_x phase rather than the proposed bimetallic phases. Such misrepresentations have contributed to the recurring appearance of erroneous structure–activity relationships in the recent literature.

Turning to the OER reaction mechanism of (doped) iridium oxides, a number of experimental and computational studies have argued that OER on iridium oxides might involve lattice oxygen sites.[8,34–36] However, the estimation of the fraction of oxygen evolved from the lattice with respect to the total amount of O_2 formed during OER proved to be an experimentally challenging task making the assignment of the dominating reaction pathway in many previous studies rather speculative.

Hence, the aim of this work is to elucidate and generalize the effect of substituents on the intrinsic activity of IrO_x derived from a series of (bi)metallic Ir-based precursors, assess *in situ* changes in the electronic and local structure of iridium sites under OER conditions, and probe the OER mechanism of IrO_x(:M) materials using electrochemical mass spectrometry (EC-MS) experiments assisted by ^{18}O-labelling. To this end, we prepared a series of monodispersed (sub-3.5 nm in diameter) bimetallic Ir–M (M = Cr, Mo, W, In) nanoparticles that serve as model catalyst precursors. We observed that there is a significant enhancement in the surface area- and iridium-mass-normalized OER activity for M = W or In (for various Ir_mIn_n and Ir_xW_y compositions). *Ex situ* XPS of the electrochemically cycled materials show that tungsten is present in the IrO_x lattice in a W^{n+} state, whereas indium is completely dissolved yielding an In-free IrO_x phase. *In situ* XAS experiments at the Ir L_3-edge allowed us to quantify the changes in the oxidation state and coordination of Ir sites during OER and to estimate the OER turnover frequency of the *in situ* formed IrO_x(:M) structures/motifs. *Operando* electrochemical mass spectrometry (EC-MS) studies using ^{18}O isotope labelling indicated that the lattice oxygen mediated mechanism (LOM) contributes to OER on all of the tested IrO_x(:M) catalysts, however the contribution of the LOM to the overall O_2 formation rate is rather small and hence cannot explain the significant differences in the intrinsic catalytic activity of the IrO_x(:M) catalysts. Instead, we established that in case of the most active catalyst, *i.e.*, IrO_x : W, the incorporation of tungsten increases the covalency of the Ir–O bonds that results in a decrease of the energy of the potential-limiting step in the conventional adsorbate-evolution mechanism (AEM). Broadly, our work targets to consolidate prior studies, providing a comprehensive perspective on the effect of substituents on the catalytic activity of iridium oxide, while also underscoring persistent challenges in the interpretation of experimental data that have led to a recurring appearance of erroneous structure–activity relationships in the recent literature.

Results and discussion

Average structural characterization of nanoparticles

Ir–M (M = Cr, Mo, W, In) nanoparticles were synthesized *via* a 1-octadecene- and oleylamine-assisted thermal decomposition of acetylacetonate- or chloride-based metal precursors (further details are provided in the SI).[37] To stabilize the $Ir^{(4-\delta)+}$ state, group VI transition metals were chosen as substituents. On the other hand, indium was selected as a substituent as the incorporation of In^{3+} is expected to yield the opposite effect, *i.e.*, to generate $Ir^{(4+\delta)+}$ sites (or, alternatively, generate oxygen vacancies). We expected that our choices of M will allow us to assess critically the findings of previous studies that have linked the presence of $Ir^{(4+\delta)+}$ or $Ir^{(4-\delta)+}$ species to an enhanced activity of various IrO_x(:M) phases.[23,24,38,39]

In the following sections, the composition of the nanoparticles will be described using the nominal Ir : M ratio used in the synthesis. The exact Ir : M composition of the nanoparticles, as determined by inductively coupled plasma optical emission spectroscopy (ICP-OES) is tabulated in Table S1. TEM and HR-STEM images of the monodispersed metallic Ir–M nanoparticles are shown in Fig. 1a, b and S1. The electron diffraction patterns of pristine Ir, $Ir_{75}W_{25}$, and $Ir_{75}In_{25}$ nanoparticles demonstrate the presence of a metallic Ir phase in all catalysts (Fig. 1c), which is in agreement with the powder X-ray diffraction patterns of the as-synthesized nanoparticles (Fig. 1d).

Overall electrochemical activity trends

The OER activity measurements of the series of Ir and Ir–M nanoparticles were performed in 0.1 M $HClO_4$ (see SI).[40] In general, all Ir–M catalysts exhibited a gradual increase of the OER current over the first *ca.* 10 CV cycles, followed by its stabilization. In the following, the OER current measured after 10 CV cycles, was used as the metric of the OER activity.

A comparison of the Ir-mass-normalized and geometric OER activities of Ir and Ir–M (M = Cr, Mo, W, In) is presented in Fig. 2a and S2. Polarization curves based on the geometric area of the electrodes for the Ir–M series are shown in Fig. S3. Among the different catalysts tested, Ir–W and Ir–In stand out due to their very high OER activity, exceeding appreciably the performance of monometallic Ir. Hence, in the following sections we will focus on rationalizing the high OER activity of the Ir–W and Ir–In based catalysts by characterizing in detail their structural and electronic properties.

Focusing on the series of Ir–W and Ir–In catalysts (*i.e.*, varying Ir : M ratios), we observed that in particular $Ir_{75}W_{25}$ and $Ir_{75}In_{25}$ show a very high Ir mass-normalized OER activity of ~1200 A g_{Ir}^{-1} (at 1.53 V_{RHE}), a value that significantly exceeds the activity of a catalyst derived from monometallic Ir nanoparticles (*ca.* 550 A g_{Ir}^{-1} at 1.53 V_{RHE}, Fig. 2b). It is important to note that the Ir mass-normalized OER activity of the monometallic Ir nanoparticles reported here is on par or even exceeds the activity of other reported IrO_x or Ir-based mixed oxides, including those commonly used as reference materials in the literature (Fig. S4).

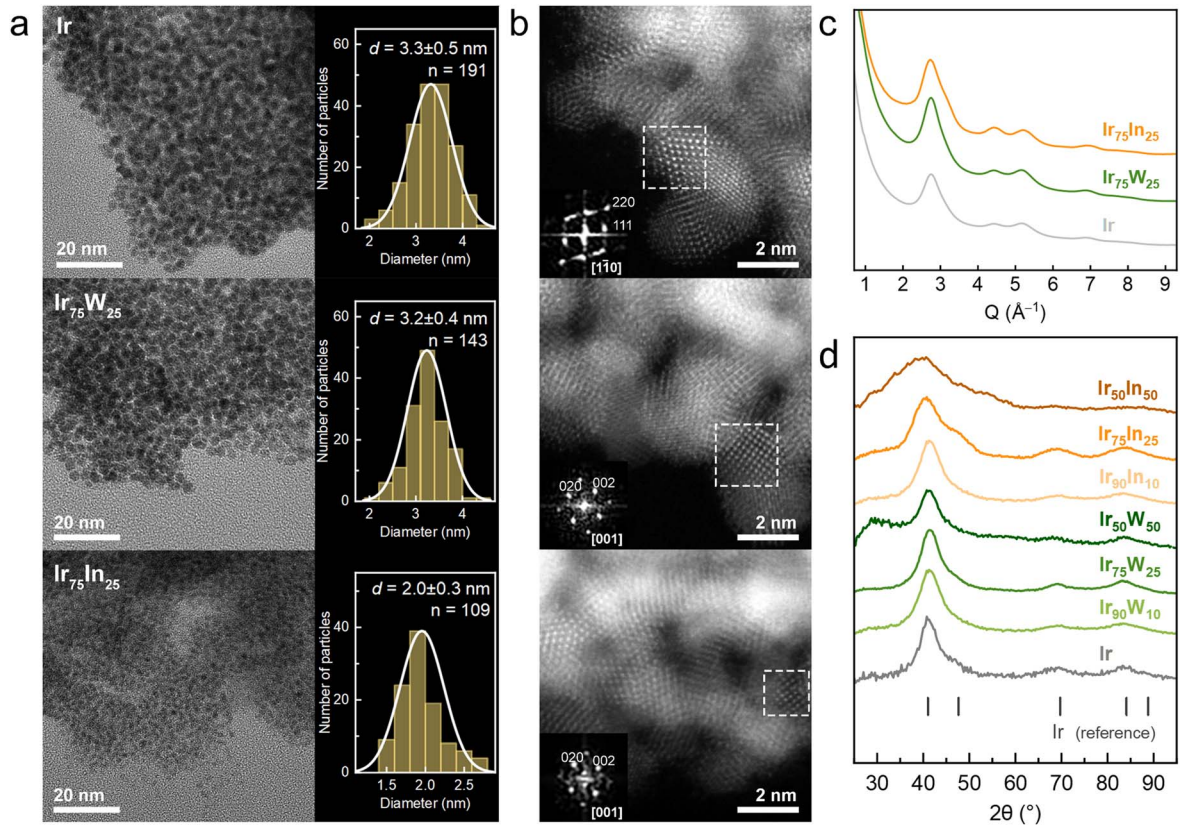

Fig. 1 (a) Bright-field transmission electron microscopy (TEM) images and the corresponding histograms of particle size distribution, (b) high-angular annular dark field scanning high-resolution transmission electron microscopy (HAADF-HRSTEM) images and the corresponding Fast Fourier Transforms (FFTs) obtained from single particles enclosed in squared areas on the HAADF-HRSTEM images, (c) azimuthally averaged intensity profiles obtained from the selected area electron diffraction (SAED) patterns of pristine Ir, $Ir_{75}W_{25}$ and $Ir_{75}In_{25}$ nanoparticles. The patterns can be indexed in the space group $Fm\bar{3}m$ (metallic Ir). (d) powder X-ray diffraction (XRD) patterns of the pristine Ir, Ir–W, and Ir–In nanoparticles (vertical lines correspond to peak positions of Ir reference [ICDD 01-071-4659]). Additional bright field TEM images of Ir–M (M = Cr, Mo, W, and In) nanoparticles are shown on Fig. S1.

Despite the similar Ir-mass-normalized OER activity of $Ir_{75}W_{25}$ and $Ir_{75}In_{25}$, the electrochemical stability of $Ir_{75}In_{25}$ was significantly inferior to that of $Ir_{75}W_{25}$ and monometallic Ir. Fig. S5 shows the first 10 cycles of cyclic voltammetry (CV) experiments of the Ir–In series for varying ratios of Ir : In. We observe a gradual decrease of the anodic current with cycle number and with increasing In content (in 0.1 M $HClO_4$). Under alkaline conditions (0.1 M KOH), there was an even faster decrease in the OER current over the first 2–3 cycles for In-rich compositions (Fig. S6). The relatively low electrocatalytic stability of the Ir–In family is also observed in Fig. 2c and can be rationalized by the high solubility of indium by forming In^{3+} or InO_2^- species (in acidic and alkaline media, respectively).[41] Interestingly, our observation differs from some previous works that report a stable and pH-independent OER activity of Ir–In based catalysts.[42]

Although the Ir-mass-normalized OER activity (A g_{Ir}^{-1}) is a frequently used metric to evaluate the activity of noble metal-based catalysts (Fig. S4), it fails to describe accurately the intrinsic activity of a catalyst (*i.e.*, the activity of an individual catalytic site). In this context, a more appropriate normalization would be based on the electrochemically active surface area (ECSA, derived from double-layer capacitance measurements; see Fig. S7) or on the geometric surface area of the nanoparticles (*e.g.*, as calculated from TEM measurements). When normalizing the OER currents by the surface area (electrochemically active surface area or geometric surface area determined by TEM), Ir–W outperforms notably the monometallic Ir catalyst, while the area-normalized OER activities of Ir–In and monometallic Ir are very similar (Fig. 2d). This comparison (Fig. 2a, d and S2) indicates that the higher Ir-mass-normalized OER current of Ir–In with respect to monometallic Ir is due to a larger number of exposed surface sites (*i.e.*, a larger electrochemically active surface area) rather than a higher intrinsic activity of the catalytically active sites (see further discussion below).

Assessment of the participation of lattice oxygen in the oxygen evolution reaction

For OER, two distinct reaction mechanisms are typically discussed, *viz.* the lattice oxygen mediated (LOM) mechanism and the (conventional) adsorbate evolution mechanism (AEM). LOM involves the coupling of neighboring oxygen sites within the oxide lattice as the O–O bond formation step, as opposed to a nucleophilic attack of H_2O/OH^- species on the terminal metal

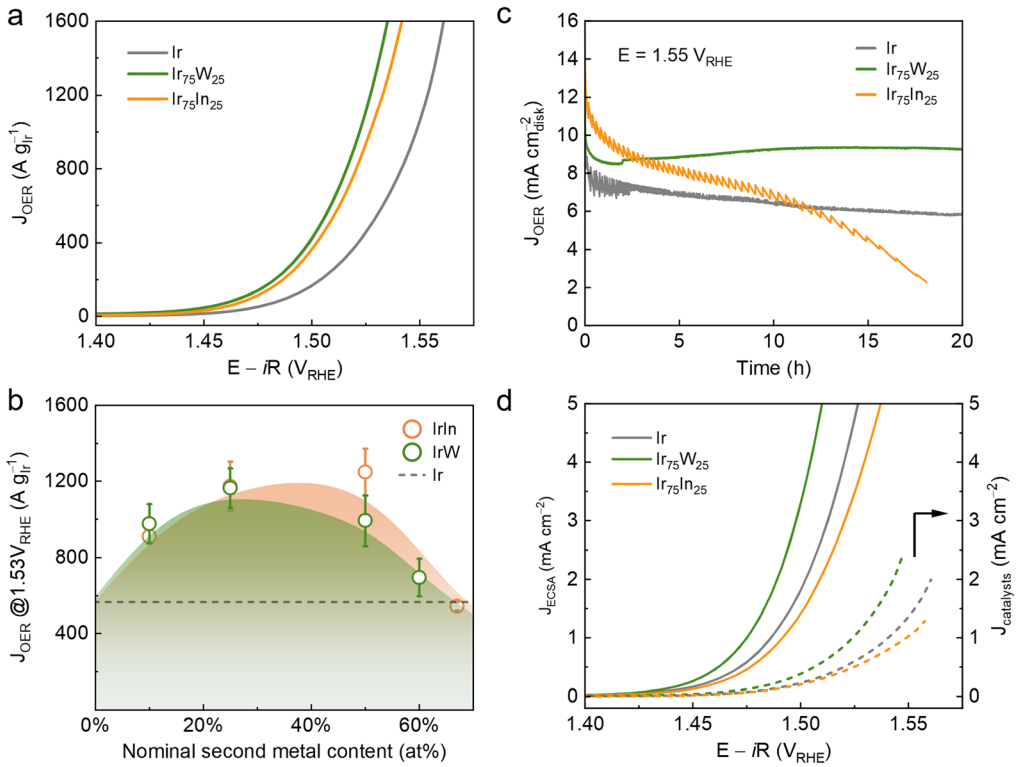

Fig. 2 (a) Ir mass-normalized polarization curves of Ir, $Ir_{75}W_{25}$, and $Ir_{75}In_{25}$ nanoparticles. (b) OER activity at 1.53 V_{RHE} for different Ir : M ratios of the Ir–W and Ir–In families. Error bars represent the standard deviations for at least seven independent measurements. (c) Chronoamperometric curves of Ir, $Ir_{75}W_{25}$, and $Ir_{75}In_{25}$ nanoparticles at 1.55 V_{RHE}. (d) Polarization curves of Ir, $Ir_{75}W_{25}$, and $Ir_{75}In_{25}$ using OER currents normalized by the electric-double-layer-derived electrochemical surface area or the total catalysts' geometric surface area (determined by TEM measurements). The catalyst loading was 10 $\mu g_{catalyst}$ cm^{-2} (except for the chronoamperometry experiments in which 50 $\mu g_{catalyst}$ cm^{-2} was used). The electrolyte was O_2-saturated 0.1 M $HClO_4$.

atoms in the AEM. It has been proposed that LOM can result in lower OER overpotentials than the AEM pathway,[43,44] hence, a large number of studies have aimed at activating the LOM by modifying the electronic structure of Ir-based catalysts. However, very few works have demonstrated experimentally that the LOM (coupling and release of lattice oxygens) indeed takes place.

To address this limitation, we investigate the involvement of lattice oxygen in the OER catalyzed by IrO_x(:M) using *operando* chip-based electrochemical mass spectrometry (EC-MS, experimental details are provided in the SI), which enables a fully quantitative analysis of the evolved gases.[45] In these experiments, first the metallic Ir–M (M = W and In) precursors were oxidized electrochemically in 0.1 M $HClO_4$–^{18}O to yield ^{18}O-enriched catalysts. After the ^{18}O-isotope-labelling step, the electrode was rinsed thoroughly with unlabeled H_2O, followed by cycling in unlabeled 0.1 M $HClO_4$ while detecting simultaneously the gas-phase products by mass spectrometry. Fig. 3a compares the evolution of the products m/z = 32 ($^{32}O_2$), 34 ($^{16}O^{18}O$), and 36 ($^{36}O_2$) during the first CV cycle as a function of time.

From Fig. 3a we observe that there is a significant production of $^{34}O_2$ ($^{16}O^{18}O$) which can be formed *via* the combination of two oxygen atoms from the electrolyte (due to the natural abundance of ^{18}O in water), *via* the combination of O atoms from the electrolyte and the oxide lattice or *via* coupling of two lattice O atoms, and $^{36}O_2$ ($^{18}O^{18}O$ formed mainly from two lattice oxygen atoms) on Ir-, $Ir_{75}W_{25}$-, and $Ir_{75}In_{25}$-derived catalysts. These measurements confirm that there is some contribution of the LOM to the overall O_2 production during OER. Fig. 3b and S8 plot the fraction of $^{32}O_2$, $^{34}O_2$ and $^{36}O_2$ in the O_2 evolved over the first 10 CV cycles for ^{18}O-labelled Ir, $Ir_{75}W_{25}$, and $Ir_{75}In_{25}$. For all materials tested, the fraction of $^{34}O_2$ gradually decreased with increasing cycle number reaching a steady-state value of ~0.55% after 5 cycles, which is close to 0.4%, *i.e.*, the expected value based on the theoretical fraction of $^{34}O_2$ evolved from water considering the natural ^{18}O abundance of 0.2%.[46] In addition, the MS signal due to $^{36}O_2$ also decreased with cycle number, falling below the detection limit after *ca.* 5 cycles, consistent with the replenishment of lattice oxygen vacancies (generated in the LOM pathway) with ^{16}O from the unlabeled electrolyte.

Hence, the main conclusions derived from our EC-MS measurements can be summarized as follows:

(1) Previous works have reported the evolution of $^{36}O_2$ from anodically oxidized ^{18}O-labelled Ir films, while crystalline rutile IrO_2 did not show any evolution of $^{36}O_2$.[34,35] Considering that we observed the evolution of $^{36}O_2$ in all of the catalysts tested, we hypothesize that the oxidized surface of all Ir–M (M = Ir, W, In) nanoparticles under OER conditions was composed of defective, hydrous IrO_x (formed also under OER conditions on a metallic Ir film) rather than of a well-defined crystalline rutile IrO_2 phase.

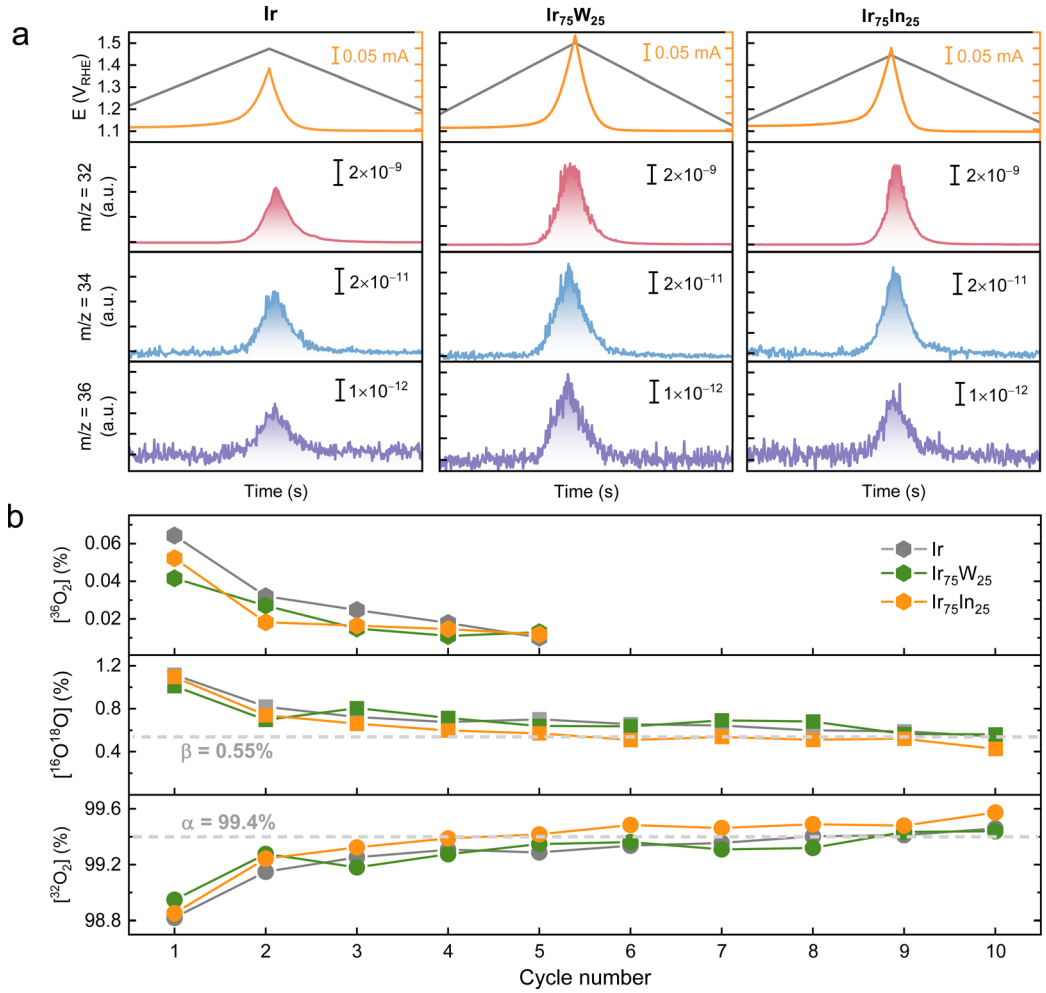

Fig. 3 (a) EC-MS profiles of the current, applied bias and MS ion currents for $m/z = 32$, 34, and 36 species as a function of time during the first OER cycle; (b) composition of the evolved O_2 species over ten OER cycles for ^{18}O-labeled Ir, $Ir_{75}W_{25}$, and $Ir_{75}In_{25}$. The dashed lines interpolate the steady state fractions of $^{32}O_2$ and $^{34}O_2$ ($^{16}O^{18}O$) when using non-labelled water (H_2O–^{16}O). Electrolyte: 0.1 M $HClO_4$ in H_2O–^{16}O. Loading: 10 $\mu g_{catalyst}$ (on a gold disk).

(2) While we observe that the OER proceeds to some extent *via* the LOM on IrO_x(:M), the quantitative analysis of the EC-MS data indicates that the fraction of O_2 formed *via* the LOM (compared to the overall amount of O_2 evolved) is rather small (Fig. S9).

(3) While we observe small differences in the fractions of $^{34}O_2$ and $^{36}O_2$ in the O_2 evolved from Ir, $Ir_{75}W_{25}$ and $Ir_{75}In_{25}$, a quantification of the different isotopes in the product (Fig. S9) indicates that the differences in the intrinsic activities observed for these three catalysts are likely not due to differences in the dominating OER mechanism (further support is provided by DFT calculations, see below).

In situ X-ray absorption spectroscopy

Next, to obtain more insight into the structure of the catalytically active sites, we used *in situ* Ir L_3 edge XAS to probe changes in the Ir oxidation state and Ir coordination environment in the IrO_x(:M) series (M = Ir, W, In) under OER conditions (we note that XAS probes the average electronic and geometric local structure of both bulk and surface Ir sites). In the *in situ* XAS experiments, the electrodes were first cycled between 0.85 V_{RHE} and 1.65 V_{RHE} (50 CV scans) to oxidize metallic iridium yielding the active IrO_x phase. Spectra collected at OCV upon immersion of the electrodes into the electrolyte are referred to as "OCV" in Fig. 4a–c, while the data collected on electrodes that have undergone 50 CV cycles are labelled "OCV (cycled)". Subsequently, chronoamperometry steps at potentials ranging from 1.16 V_{RHE} to 1.56 V_{RHE} were performed. The *in situ* X-ray absorption near edge structure (XANES) and the magnitude of the Fourier transform (FT) of the extended X-ray absorption fine structure (EXAFS) data of Ir, $Ir_{75}W_{25}$, $Ir_{75}In_{25}$ and $Ir_{50}In_{50}$ are shown in Fig. 4a and b. The XANES data of further Ir–W compositions are presented in Fig. S10. The white line (WL) peak position (fitted using one Lorentzian component) was selected as the parameter to estimate the oxidation state of iridium in the catalysts (Fig. S11), instead of using the integrated intensity (see discussion in the SI).

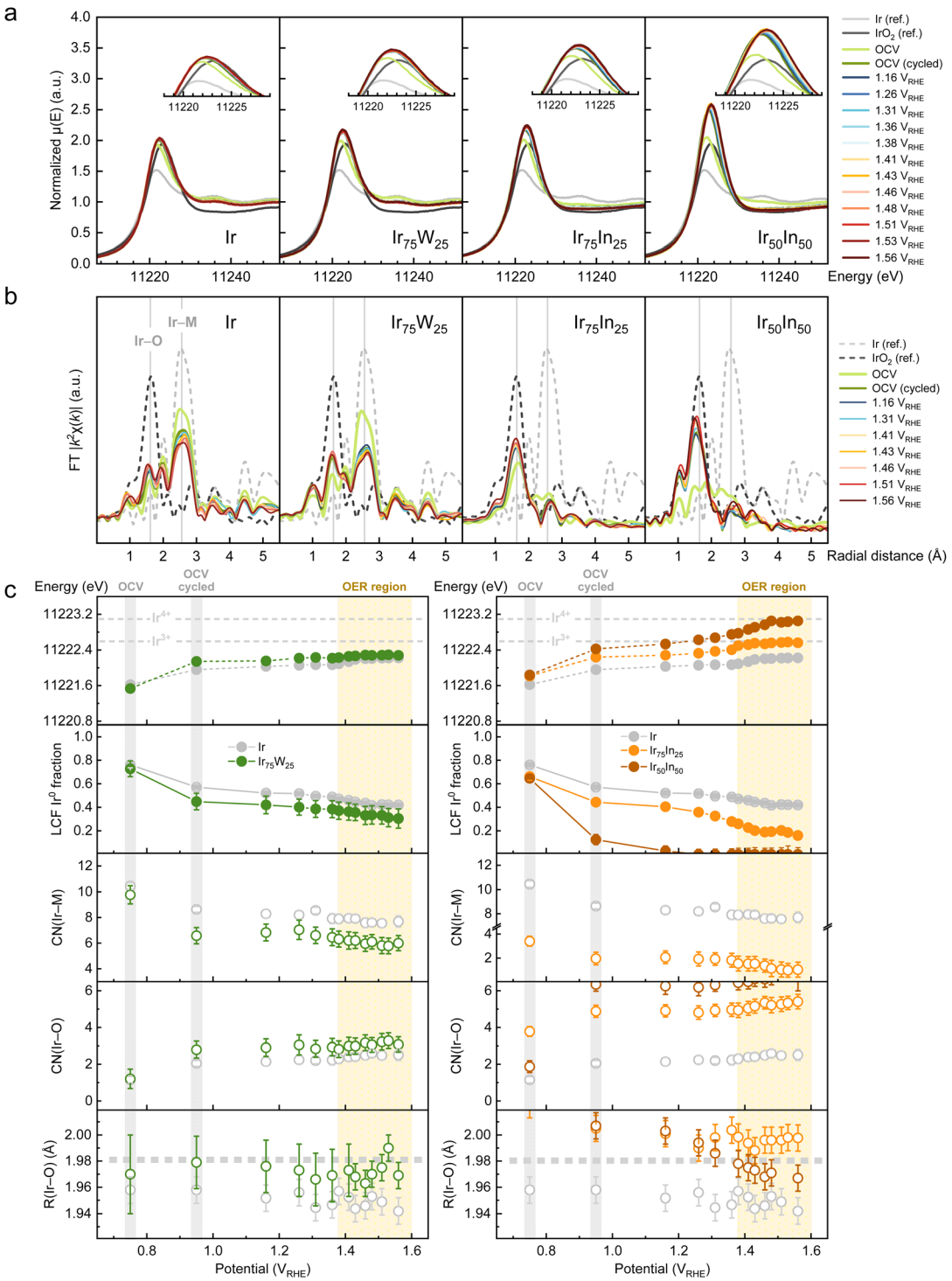

Fig. 4 *In situ* (a) XANES and (b) non-phase-shift corrected k^2-weighted magnitude of the FT EXAFS, at different stages of CV cycling and during chronoamperometric steps of Ir, $Ir_{75}W_{25}$, $Ir_{75}In_{25}$, and $Ir_{50}In_{50}$. (c) Ir L_3-edge WL position, Ir^0 fraction derived from linear combination fitting (references: Ir powder, Ir(acac)$_3$ and IrO_2), fitted Ir–M and Ir–O coordination numbers, fitted Ir–O interatomic distance of Ir, $Ir_{75}W_{25}$, $Ir_{75}In_{25}$ and $Ir_{50}In_{50}$ as a function of the applied potential in 0.1 M $HClO_4$ using a static cell. The bottom baseline of the first panel of (c) indicates the peak position of the fitted metallic Ir reference (11 220.72 eV). All spectra were acquired in fluorescence mode, except of that of the references Ir, Ir(acac)$_3$, and IrO_2. Error bars represent the uncertainties in the fit variables. The EXAFS fitting parameters can be found in Table S2. Loading: 2 $mg_{catalyst}$ cm^{-2} (on carbon paper).

Evolution of the fraction of IrO_x and the average oxidation state of Ir under OER conditions

When comparing the XANES spectra of Ir, $Ir_{75}W_{25}$, $Ir_{75}In_{25}$, $Ir_{50}In_{50}$ before and after cycling, we observe a shift in the peak position of the white line (WL) to higher energies, along with an increase in the intensity of the WL (Fig. 4a–c and S11). This observation indicates that the average oxidation state of iridium in Ir, Ir–W and Ir–In catalysts increases with CV cycling which we attribute to the formation of oxidized Ir species (*i.e.*, IrO_x) during the initial 50 CV cycles (consistent with the *ex situ* X-ray photoelectron Ir 4f core spectra (XPS) of the materials, Fig. S12).

The shift in the WL energy position during the chronoamperometric steps can be due to (i) a further oxidation of the remaining metallic Ir^0 core to generate additional IrO_x species and/or (ii) an increase of the oxidation state of Ir in the already formed IrO_x phase. To disentangle these two potential contributions, we monitor the fraction of metallic Ir^0 of Ir, $Ir_{75}W_{25}$, $Ir_{75}In_{25}$ and $Ir_{50}In_{50}$ after cycling and during the chronoamperometric steps using linear combination fitting (LCF) analysis (details in the SI). While determining the exact oxidation state of Ir in the IrO_x phase by XANES is very challenging due to the overlapping features of Ir species of different oxidation states, our analysis, nonetheless, allowed us to follow the evolution of the non-Ir^0 (*i.e.*, IrO_x) component as a function of the applied potential. LCF analysis revealed that the fraction of Ir^0 decreased during cycling and, to a lesser extent, during the step chronoamperometry experiments, independent of the catalyst formulation.

During the chronoamperometric steps, the decrease in the fraction of Ir^0 was most pronounced in Ir–In (in particular for $Ir_{50}In_{50}$) and less noticeable in Ir and $Ir_{75}W_{25}$ (Fig. 4a and c). Specifically, between the state "OCV (cycled)" and "1.56 V_{RHE}", the fraction of Ir^0 decreased from 0.57 to 0.42 for Ir, from 0.44 to 0.30 for $Ir_{75}W_{25}$, and from 0.45 to 0.16 for $Ir_{75}In_{25}$. For $Ir_{50}In_{50}$, the fraction of Ir^0 reduced to zero indicating the complete oxidation of metallic Ir during the step chronoamperometric experiments. We speculate that the oxidation of a larger fraction of the original Ir^0 phase in Ir–In-based catalysts is due to (i) the smaller size of the Ir–In nanoparticles (when compared to the Ir and Ir–W samples), resulting in a higher fraction of surface Ir sites exposed to the electrolyte and (ii) due to the rapid dissolution of In in acidic electrolytes (consistent with the Pourbaix diagram for In–H_2O[41]), as also confirmed by *ex situ* XPS that showed the absence of In in the cycled material (Fig. S13).

In contrast to the Ir–In series in which In was leached out completely, W remained as a mixture of +4, +5 and +6 states (as probed by the *ex situ* XPS studies) in the structure of the Ir–W catalysts. Furthermore, our W L_3-edge EXAFS data suggest that W has a local environment and R(W–O) that are distinct from that of WO_2 or WO_3 (Fig. S14) (note that due to the restriction of the *k*-range to *ca.* 9 Å, the structural analysis was confined to the W–O coordination shell). While the XAS data do not allow an unambiguous determination of the exact geometry of the W sites in IrO_x:W, our observations support a structural model in which (i) WO_x is dispersed within the IrO_x matrix (in the bulk or at the surface of IrO_x), and (ii) there is an electronic interaction between W and Ir (hence pointing to a Ir–O–W bonding). Considering all experimental data acquired, we therefore argue that the incorporation of W into the IrO_x crystal lattice represents the most likely structural model, which was therefore used in the DFT calculations (see below).

Evolution of the local structure of the catalysts as probed by EXAFS

Next, we performed EXAFS fittings to determine the average coordination numbers (CN) and interatomic distances (*R*) of the Ir–O and Ir–M (M = Ir, W, or In) coordination shells (Fig. 4c, S15, S16, and Table S2; see also Fig. S17 for *in situ* k^2-weighted EXAFS data in *k*-space of Ir, Ir–W and Ir–In catalysts). Comparing the structure of the catalysts before and after cycling, we find that the CN of the Ir–M shell decreased for all materials tested (see Table S2). In addition, after the chronoamperometric steps up to 1.56 V_{RHE}, the CN(Ir–M) decreased even further to 7.5(4) in Ir, to 6.2(5) in $Ir_{75}W_{25}$ and to 0.9(5) $Ir_{75}In_{25}$ (Fig. 4c). In $Ir_{50}In_{50}$ the magnitude of the Ir–M shell was negligible after the chronoamperometric steps up to 1.56 V_{RHE}, consistent with LCF analysis that showed the absence of a metallic Ir^0 phase. Furthermore, the decrease of the CN(Ir–M) is accompanied by an increase in the corresponding CN(Ir–O) (see Table S2), which is consistent with the reduction of the fraction of Ir^0 and the formation of an IrO_x phase during CV cycling and the subsequent chronoamperometric steps.

Turning now to the fitted interatomic distances, the *R*(Ir–M) in the Ir and Ir–W catalysts studied here, fluctuate around 2.7 Å (Fig. S15) throughout the duration of the *in situ* experiments, in good agreement with *R*(Ir–Ir) = 2.704(5) Å in the reference Ir powder (Sigma-Aldrich). This observation implies that in the Ir and Ir–W catalysts a metallic iridium core is preserved to some extent during the *in situ* electrochemical experiment.

Previous reports probing the structure of the active iridium oxide/(oxy)hydroxide phases report a shortening of *R*(Ir–O) at increasing OER potentials and link the decrease in *R*(Ir–O) with an increase in the oxidation state of iridium.[47] At "OCV (cycled)", the shorter *R*(Ir–O) of the IrO_x phase formed in the monometallic Ir precursor (*R*(Ir–O) = 1.958(8) Å) when compared to the Ir^{4+} reference IrO_2 (*R*(Ir–O) = 1.983 Å) suggests a higher (average) oxidation state of the iridium sites of the IrO_x phase in the monometallic Ir catalyst (*i.e.*, $Ir^{(4+\delta)+}$) compared to crystalline IrO_2.[48] Indeed, when comparing *R*(Ir–O) of the IrO_x phase obtained from the monometallic Ir precursor after the chronoamperometric steps (1.94(1) Å at 1.56 V_{RHE}) and an anodically oxidized IrO_x film (1.94 Å at 1.0 $V_{Ag/AgCl}$),[47] suggests that the oxidation state of Ir in these two materials is very similar (*i.e.*, *ca.* $Ir^{4.5+}$). On the other hand, *R*(Ir–O) in IrO_x:W formed at the "OCV(cycled)" stage from $Ir_{75}W_{25}$ is close to that of crystalline IrO_2 (Fig. 4c).

In the Ir–In system, *R*(Ir–O) at "OCV (cycled)" is larger than the respective values of the monometallic Ir-derived catalysts which we attribute to a lower oxidation state of Ir in the IrO_x phases derived from Ir–In precursors (*i.e.*, Ir^{4+} or $Ir^{(4-\delta)+}$). Application of a bias (up to 1.56 V_{RHE}) resulted in insignificant changes in the mean oxidation state of the IrO_x phase derived from $Ir_{75}In_{25}$ and the formation of $Ir^{4+}O_x(OH)_y$ from the $Ir_{50}In_{50}$

precursor (bottom panel of Fig. 4c). We speculate that the relatively low oxidation state of iridium in the catalysts formed from the Ir–W and Ir–In precursors is caused by, respectively, (i) the substitution of Ir with high-valence W resulting in a reduction of Ir and (ii) the loss of indium which facilitates the formation of a defective (*i.e.*, oxygen vacancy-rich) IrO_x phase.

The structural difference between the IrO_x phase formed in Ir–In (in particular for higher In contents) and crystalline IrO_2 is also seen qualitatively in the FT EXAFS data. While the crystalline IrO_2 reference shows a peak at *ca.* 3.5 Å (without phase-shift correction, Fig. 4b) which is expected for a higher-order Ir–Ir coordination in crystalline Ir oxides, this peak is absent in the FT EXAFS of the Ir–In system both at "OCV (cycled)" and during the chronoamperometric steps. These observations suggest that IrO_x derived from $Ir_{75}In_{25}$ and $Ir_{50}In_{50}$ nanoparticles (upon loss of In from the lattice) lacks the long-range order that is characteristic of rutile IrO_2.

To conclude, *in situ* XAS analysis allowed us (i) to probe changes in the average oxidation state of iridium, (ii) determine the fraction of Ir^0 converted into IrO_x at the various steps of the *in situ* experiment, and (iii) determine the local environment of the iridium sites in the *in situ* formed IrO_x(:M) phases. We observed that at OER potentials iridium in the IrO_x phase obtained in the monometallic Ir system has an oxidation state ~+4.5, whereas the oxidation state of iridium is ~+4 in IrO_x:W. We attribute this effect to the presence of high oxidation state W in the IrO_x structure. In the Ir–In system, the leaching of In resulted in the complete oxidation of metallic iridium forming a defective IrO_x phase that lacks long range order and in which the oxidation state of Ir at OER potentials does not exceed +4.

Intrinsic activity of the IrO_x phase formed *in situ* from the different bimetallic precursors

Next, we compare the intrinsic OER activities of the Ir, Ir–In and Ir–W catalysts which we define as the OER current normalized by the mass of the electrochemically active sites (*i.e.*, the mass of *in situ* formed IrO_x), determined by LCF analysis of the data collected at OCV after the chronoamperometric steps (see also Fig. S18). Using LCF analysis, at the end of the *in situ* electrochemical experiment the following fractions of IrO_x were determined: 50% (Ir), 65% ($Ir_{75}W_{25}$), 81% ($Ir_{75}In_{25}$), and 100% ($Ir_{50}In_{50}$). Calculating the IrO_x-mass-normalized OER currents, we find that the activities of Ir, $Ir_{75}In_{25}$ and $Ir_{50}In_{50}$ are very similar (*ca.* 400 A $g_{Ir\rightarrow IrO_x}^{-1}$ at 1.50 V_{RHE}, Fig. 5a). However, the IrO_x-mass-normalized OER activity of $Ir_{75}W_{25}$ is much higher, *i.e.*, 650 A $g_{Ir\rightarrow IrO_x}^{-1}$ at 1.50 V_{RHE}. It is worth noting that the OER activity of the monometallic Ir catalyst studied here is comparable or even exceeding the Ir-mass-normalized activity when compared to previously reported iridium oxides/alloys (Fig. S4). Therefore, the ~60% higher intrinsic OER activity of Ir–W compared to monometallic Ir represents a significant improvement.

Quantifying the fraction of IrO_x also allowed us to estimate the turnover frequency (TOF) of the IrO_x:M catalysts (further details in the SI, Table S3). In the following we calculate and report three differently defined TOFs:

(1) $TOF_{surface}$: calculated by normalizing the OER current to the total geometric surface area of the nanoparticles determined by TEM (serving as an upper boundary);

(2) TOF_{bulk}: calculated by normalizing the OER current to the total loading of Ir on the electrode (serving as a lower boundary);

(3) TOF_{EA}: calculated by normalizing the OER current to the mass of the electrochemically active iridium (*i.e.*, the amount of IrO_x determined by LCF analysis).

The following values of TOF_{EA} were determined: 0.18 s^{-1} (Ir), 0.34 s^{-1} ($Ir_{75}W_{25}$), and 0.20 s^{-1} ($Ir_{75}In_{25}$) at 1.50 V_{RHE} and 0.57 s^{-1} (Ir), 1.05 s^{-1} ($Ir_{75}W_{25}$), 0.59 s^{-1} ($Ir_{75}In_{25}$) at 1.53 V_{RHE} (Fig. 5b). It is noticeable that TOF_{EA} of the catalysts that are derived from monometallic Ir and $Ir_{75}In_{25}$ nanoparticles are very similar implying that the structural differences between the IrO_x phases formed from the Ir and Ir–In precursors

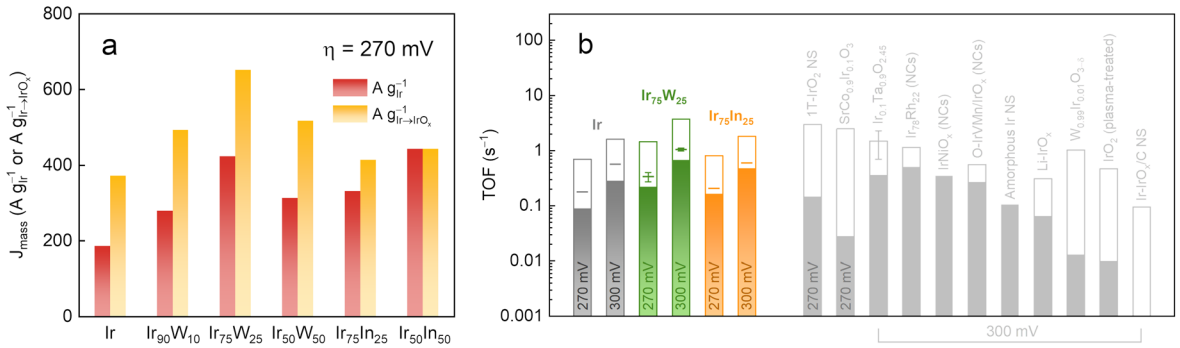

Fig. 5 (a) Intrinsic OER activity at 1.50 V_{RHE} normalized by the total Ir mass loading or the LCF-derived fraction of IrO_x. (b) Comparison of the turnover frequency (TOF) of the catalyst series studied here with selected, previously reported Ir-based catalysts in acid conditions at different overpotentials. The error bars for $Ir_{75}W_{25}$ catalyst correspond to uncertainty in the fraction of IrO_2-component in LCF analysis. Empty bars: $TOF_{surface}$ (based on catalyst surface area except for $W_{0.99}Ir_{001}O_{3-\delta}$ and IrO_2 (plasma-treated)[31] for which the TOFs are based on the reported amount of Ir atoms at the catalyst surface); filled bars: TOF_{bulk} (based on total Ir loading). TOF_{EA} indexed by straight line (–) was calculated using the fraction of IrO_x present after the *in situ* XAS experiments. Some TOFs from literature were re-calculated using the reported particle size, Ir content, catalyst loading, Brunauer–Emmett–Teller (BET) or TEM-determined surface area.[32,49–51] (NCs: nanoparticles. NS: nanosheets). The exact values are listed in Table S3.

(specifically, the lack of a long-range order for the latter) have a rather small impact on the intrinsic activity of the catalytically active iridium sites (Fig. 2c). Hence, we can also conclude that the markedly higher geometric activity (mA cm_{disk}^{-2}) and total Ir mass activity (A g_{Ir}^{-1}) of the Ir–In catalysts, relative to monometallic Ir, arise exclusively from the larger surface area and the greater fraction of Ir converted into IrO_x in the Ir–In system.

Remarkably, the TOF_{EA} of $Ir_{75}W_{25}$ is comparable to that of two-dimensional iridium oxide (0.15 s^{-1} at 1.50 V_{RHE}) and $Ir_{0.1}Ta_{0.9}O_{2.45}$ (1.5 ± 0.8 s^{-1} at 1.53 V_{RHE}, fraction of the catalytically active sites was estimated by ^{13}CO stripping measurements), *i.e.*, placing it among the best performing OER catalysts (Fig. 5b and Table S3).[2,52] Even when using the TOF values that do not account for the fraction of the electrochemically active IrO_x (*i.e.*, TOF_{bulk}: 0.22 s^{-1} at 1.50 V_{RHE} and 0.68 s^{-1} at 1.53 V_{RHE}), $Ir_{75}W_{25}$ exceeds the performance of many state-of-the-art Ir-based electrocatalysts (Fig. 5b and Table S3),[2,6,31,49–56] indicative that the addition of W yields an exceptionally active OER catalyst.

Origin of the enhanced activity of IrO_x:W catalysts: theoretical considerations

The combined EC-MS and *in situ* XAS studies indicate that the enhanced OER activity of IrO_x:W does not originate from a switch of the reaction mechanism from the AEM to the LOM pathway. To add a theoretical support and rationalize this observation, we performed DFT calculations of the energetics of different OER pathways (*i.e.*, the conventional AEM, LOM and I2M [coupling of two oxo-moieties bound to neighboring metal sites] pathways) on both IrO_2 and W-substituted IrO_2 (110) surfaces (Fig. 6a). The schematics of the proposed reaction mechanisms and the respective computed Gibbs free energy diagrams are shown in Fig. 6b, S19, S20, and Table S4. While we recognize that the ideal rutile IrO_2 model does not explicitly reproduce the structural complexity of the catalytically active hydrous IrO_x phase, it nonetheless provides a valid framework to assess the impact of tungsten incorporation on the energetics of OER intermediates in the IrO_x system.

We observed that the potential-determining step of the AEM over IrO_2(:W) is the step *OOH → * + O_2; this is consistent with previous theoretical OER studies on iridium oxides.[36,57] The incorporation of W in the IrO_2 lattice decreases the free energy difference of this step (*i.e.*, it becomes less endothermic) resulting in turn in a decrease of the theoretical OER overpotential in both W-containing models. Consistent with our measurements and previous literature reports,[35] our calculations indicate that the contribution of lattice oxygen *via* LOM is rather small for IrO_2 as it requires significantly larger OER overpotentials as compared to the AEM; similarly, I2M pathway was also found to be not feasible for the studied model systems (Fig. S19, S20 and Table S4).

To probe the effect of tungsten substitution on the electronic properties of IrO_2:W, we calculated the electronic band structure and the Bader charges for the three models shown on

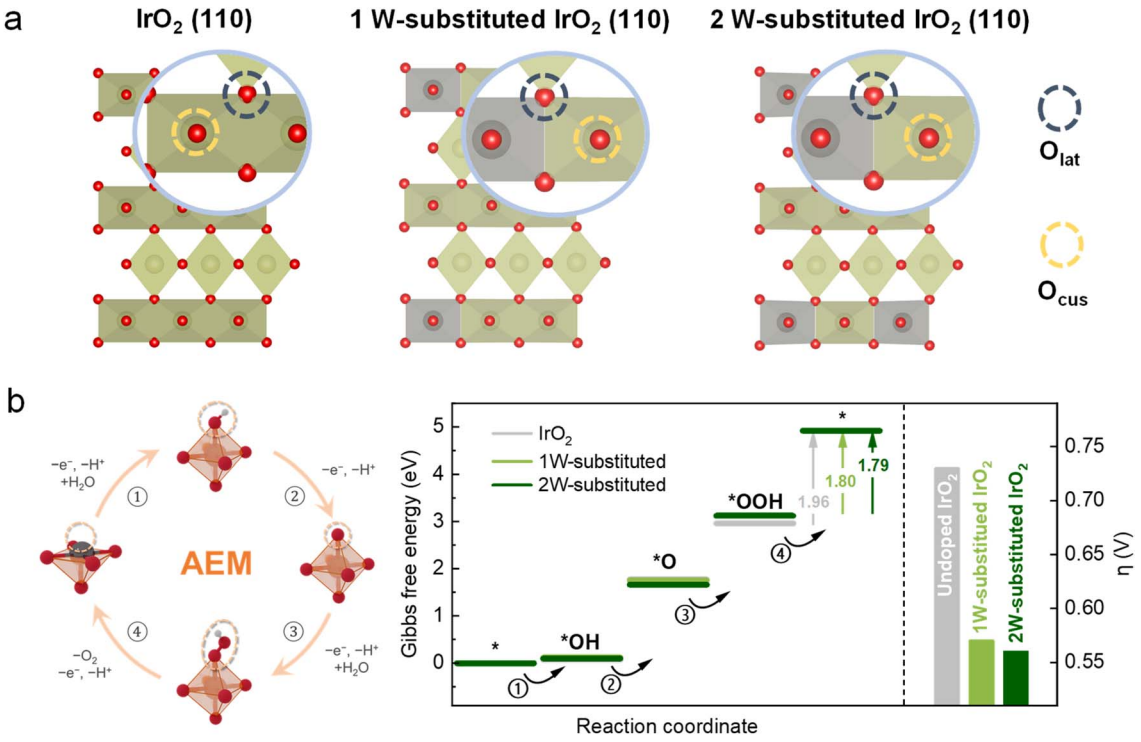

Fig. 6 (a) Top view of the (110) termination of unsubstituted IrO_2, and IrO_2 containing one or two W atoms replacing iridium sites on the surface. These models were used in the DFT calculations. Highlighted are the bridging lattice oxygen (O_{lat}) and coordinatively unsaturated (O_{cus}) oxygen sites. (b) Schematic representation of the adsorbate evolution mechanism (AEM) of the OER considered in the DFT calculations and the corresponding Gibbs free energy diagram of the four elementary steps computed for each model shown on panel (a).

Fig. 6a, S21 and Table S5. We found that the substitution of iridium with tungsten resulted in a decrease of the Bader charges on the Ir sites (*i.e.*, from 1.88 for unsubstituted IrO_2 to 1.82–1.83 for W-substituted IrO_2), consistent with the *in situ* XAS observed reduction of the average oxidation state of iridium in $Ir_{75}W_{25}$. Such redistribution of charges, induced by the inductive effect of W[58] renders Ir–O bond more covalent that is reflected in a reduced energy gap between the Ir 5d and O 2p band centers for the W-substituted models, when compared to unsubstituted IrO_2 (Table S5). Therefore, a significantly higher intrinsic activity (*i.e.*, TOF) of IrO_x:W derived from Ir–W precursors, relative to monometallic IrO_x, can be primarily ascribed to a W-induced electronic effect on adjacent O/Ir sites. This change in covalency of the Ir–O bond affects the adsorption energies of the O-containing OER intermediates and hence the overall OER kinetics.

Conclusions

This work demonstrates that substituting Ir with W or In yields OER catalysts with significantly higher OER activity than bulk IrO_2 or previously reported Ir-based catalysts. Using a series of complementary characterization techniques including *in situ* XAS and *operando* EC-MS analysis we rationalize the origin of the different (intrinsic) OER activities of IrO_x derived from different Ir(–M) precursors. The higher total iridium mass normalized OER activity of Ir–In compared to Ir originates from a higher fraction of the electrochemically (catalytically) active sites. On the other hand, IrO_x:W derived from Ir–W precursors exhibits a significantly higher TOF (*i.e.*, intrinsic activity) than the monometallic IrO_x phase. This is attributed to a W-induced electronic effect on neighboring O/Ir sites. In all Ir-based catalysts studied here, EC-MS experiments confirm the participation of lattice oxygen atoms in OER, however there was no noticeable difference in the extent of lattice oxygen evolution between the different IrO_x:M catalysts. DFT calculations attribute the increase of the OER activity upon partial substitution of Ir by W to an increased covalency of the Ir–O bonds resulting in a decrease of the energy of the potential-limiting step in the AEM pathway rather than an activation of the LOM. Overall, the work reported here introduces novel, highly active OER catalysts, rationalizes the origin of their improved activity and demonstrates the importance of an accurate quantitative assessment of the intrinsic activity of IrO_x-based catalysts to yield robust structure–activity correlations that can aid the rational design of new compositions for acidic water electrolysis.

Author contributions

Y. X. and Y.-H. W. synthesized materials and performed electrochemical measurements. Y.-H. W. performed XPS characterizations. D. P. performed HR-STEM imaging and EDX analysis. A. K. collected TEM images and performed ICP-OES anaylsis. P. C. and V. A. performed DFT calculations. Y. X., Y.-H. W. and D. A. K. performed XAS. Y.-H. W and P. M. A. process XAS data analysis with input from C. S. and V. C. D. A. K. and C. R. M. supervised the research. The manuscript was edited by all authors.

Conflicts of interest

There are no conflicts to declare.

Data availability

The data supporting this article have been included as part of the supplementary information (SI). Supplementary information is available. See DOI: **https://doi.org/10.1039/d5sc06242j**.

Acknowledgements

The authors acknowledge the Swiss Federal Laboratories for Materials Science and Technology (EMPA) for access to the XPS facility, the Diamond Light Source for access to the synchrotron radiation facilities at the B18 beamlines, and ScopeM (ETH Zürich) for access to the electron microscopy facilities. Harshit Mehta and Arthur Thevenot are acknowledged for participation in the optimization of the synthesis methods. Valentina Vogt and Alexander Oing are thanked for their participation in synchrotron XAS experiments. Y. X. acknowledges the support provided by Prof. D. Tilley. The authors are grateful to Prof. Dimos Poulikakos for his continuous support and encouragement. D. P. acknowledges the financial support of the Swiss National Science Foundation (SNSF) within the Swiss Postdoctoral Fellowship (grant no. TMPFP2_224646). The Swiss National Science Foundation (grant no. 200021_196943/1) and the Swiss Office of Energy (grant no. S1/502898–01) are acknowledged for financial support. This work was created as part of NCCR Catalysis (grant no. 180544), a National Centre of Competence in Research funded by the Swiss National Science Foundation.

References

1 T. Reier, M. Oezaslan and P. Strasser, *ACS Catal.*, 2012, **2**, 1765–1772.
2 Y.-R. Zheng, J. Vernieres, Z. Wang, K. Zhang, D. Hochfilzer, K. Krempl, T.-W. Liao, F. Presel, T. Altantzis, J. Fatermans, S. B. Scott, N. M. Secher, C. Moon, P. Liu, S. Bals, S. Van Aert, A. Cao, M. Anand, J. K. Nørskov, J. Kibsgaard and I. Chorkendorff, *Nat. Energy*, 2021, **7**, 55–64.
3 S. Cherevko, S. Geiger, O. Kasian, N. Kulyk, J.-P. Grote, A. Savan, B. R. Shrestha, S. Merzlikin, B. Breitbach, A. Ludwig and K. J. J. Mayrhofer, *Catal. Today*, 2016, **262**, 170–180.
4 D. Y. Kuo, J. K. Kawasaki, J. N. Nelson, J. Kloppenburg, G. Hautier, K. M. Shen, D. G. Schlom and J. Suntivich, *J. Am. Chem. Soc.*, 2017, **139**, 3473–3479.
5 H. N. Nong, L. J. Falling, A. Bergmann, M. Klingenhof, H. P. Tran, C. Spori, R. Mom, J. Timoshenko, G. Zichittella, A. Knop-Gericke, S. Piccinin, J. Perez-Ramirez, B. R. Cuenya, R. Schlogl, P. Strasser, D. Teschner and T. E. Jones, *Nature*, 2020, **587**, 408–413.

6 H. N. Nong, T. Reier, H.-S. Oh, M. Gliech, P. Paciok, T. H. T. Vu, D. Teschner, M. Heggen, V. Petkov, R. Schlögl, T. Jones and P. Strasser, *Nat. Catal.*, 2018, **1**, 841–851.
7 Y. Lee, J. Suntivich, K. J. May, E. E. Perry and Y. Shao-Horn, *J. Phys. Chem. Lett.*, 2012, **3**, 399–404.
8 S. B. Scott, J. E. Sorensen, R. R. Rao, C. Moon, J. Kibsgaard, Y. Shao-Horn and I. Chorkendorff, *Energy Environ. Sci.*, 2022, **15**, 1988–2001.
9 C. Liang, R. R. Rao, K. L. Svane, J. H. L. Hadden, B. Moss, S. B. Scott, M. Sachs, J. Murawski, A. M. Frandsen, D. J. Riley, M. P. Ryan, J. Rossmeisl, J. R. Durrant and I. E. L. Stephens, *Nat. Catal.*, 2024, **7**, 763–775.
10 D. F. Abbott, D. Lebedev, K. Waltar, M. Povia, M. Nachtegaal, E. Fabbri, C. Copéret and T. J. Schmidt, *Chem. Mater.*, 2016, **28**, 6591–6604.
11 S. Geiger, O. Kasian, B. R. Shrestha, A. M. Mingers, K. J. J. Mayrhofer and S. Cherevko, *J. Electrochem. Soc.*, 2016, **163**, F3132–F3138.
12 S. Cherevko, A. R. Zeradjanin, A. A. Topalov, N. Kulyk, I. Katsounaros and K. J. J. Mayrhofer, *ChemCatChem*, 2014, **6**, 2219–2223.
13 O. Schmidt, A. Gambhir, I. Staffell, A. Hawkes, J. Nelson and S. Few, *Int. J. Hydrogen Energy*, 2017, **42**, 30470–30492.
14 L. C. Seitz, C. F. Dickens, K. Nishio, Y. Hikita, J. Montoya, A. Doyle, C. Kirk, A. Vojvodic, H. Y. Hwang and J. K. Norskov, *Science*, 2016, **353**, 1011–1014.
15 O. Diaz-Morales, S. Raaijman, R. Kortlever, P. J. Kooyman, T. Wezendonk, J. Gascon, W. T. Fu and M. T. Koper, *Nat. Commun.*, 2016, **7**, 12363.
16 D. Lebedev, M. Povia, K. Waltar, P. M. Abdala, I. E. Castelli, E. Fabbri, M. V. Blanco, A. Fedorov, C. Copéret and N. Marzari, *Chem. Mater.*, 2017, **29**, 5182–5191.
17 G. Wan, J. W. Freeland, J. Kloppenburg, G. Petretto, J. N. Nelson, D.-Y. Kuo, C.-J. Sun, J. Wen, J. T. Diulus, G. S. Herman, Y. Dong, R. Kou, J. Sun, S. Chen, K. M. Shen, D. G. Schlom, G.-M. Rignanese, G. Hautier, D. D. Fong, Z. Feng, H. Zhou and J. Suntivich, *Sci. Adv.*, 2021, **7**, eabc7323.
18 R. Zhang, N. Dubouis, M. Ben Osman, W. Yin, M. T. Sougrati, D. A. D. Corte, D. Giaume and A. Grimaud, *Angew Chem. Int. Ed. Engl.*, 2019, **58**, 4571–4575.
19 S. Geiger, O. Kasian, M. Ledendecker, E. Pizzutilo, A. M. Mingers, W. T. Fu, O. Diaz-Morales, Z. Li, T. Oellers, L. Fruchter, A. Ludwig, K. J. J. Mayrhofer, M. T. M. Koper and S. Cherevko, *Nat. Catal.*, 2018, **1**, 508–515.
20 L. C. Seitz, C. F. Dickens, K. Nishio, Y. Hikita, J. Montoya, A. Doyle, C. Kirk, A. Vojvodic, H. Y. Hwang, J. K. Norskov and T. F. Jaramillo, *Science*, 2016, **353**, 1011–1014.
21 A. Grimaud, A. Demortière, M. Saubanère, W. Dachraoui, M. Duchamp, M.-L. Doublet and J.-M. Tarascon, *Nat. Energy*, 2016, **2**, 16189.
22 C. W. Song, J. Lim, H. B. Bae and S.-Y. Chung, *Energy Environ. Sci.*, 2020, **13**, 4178–4188.
23 A. Minguzzi, O. Lugaresi, E. Achilli, C. Locatelli, A. Vertova, P. Ghigna and S. Rondinini, *Chem. Sci.*, 2014, **5**, 3591–3597.
24 V. Pfeifer, T. E. Jones, J. J. Velasco Velez, C. Massue, M. T. Greiner, R. Arrigo, D. Teschner, F. Girgsdies, M. Scherzer, J. Allan, M. Hashagen, G. Weinberg, S. Piccinin, M. Havecker, A. Knop-Gericke and R. Schlögl, *Phys. Chem. Chem. Phys.*, 2016, **18**, 2292–2296.
25 Z. Pavlovic, C. Ranjan, M. van Gastel and R. Schlogl, *Chem. Commun.*, 2017, **53**, 12414–12417.
26 E. Willinger, C. Massue, R. Schlogl and M. G. Willinger, *J. Am. Chem. Soc.*, 2017, **139**, 12093–12101.
27 C. Daiane Ferreira da Silva, F. Claudel, V. Martin, R. Chattot, S. Abbou, K. Kumar, I. Jiménez-Morales, S. Cavaliere, D. Jones, J. Rozière, L. Solà-Hernandez, C. Beauger, M. Faustini, J. Peron, B. Gilles, T. Encinas, L. Piccolo, F. H. Barros de Lima, L. Dubau and F. Maillard, *ACS Catal.*, 2021, **11**, 4107–4116.
28 V. Pfeifer, T. E. Jones, J. J. Velasco Velez, R. Arrigo, S. Piccinin, M. Havecker, A. Knop-Gericke and R. Schlogl, *Chem. Sci.*, 2017, **8**, 2143–2149.
29 B. Lu, C. Wahl, R. dos Reis, J. Edgington, X. K. Lu, R. Li, M. E. Sweers, B. Ruggiero, G. T. K. K. Gunasooriya, V. Dravid and L. C. Seitz, *Nat. Catal.*, 2024, **7**, 868–877.
30 P. Lettenmeier, L. Wang, U. Golla-Schindler, P. Gazdzicki, N. A. Canas, M. Handl, R. Hiesgen, S. S. Hosseiny, A. S. Gago and K. A. Friedrich, *Angew Chem. Int. Ed. Engl.*, 2016, **55**, 742–746.
31 S. Kumari, B. P. Ajayi, B. Kumar, J. B. Jasinski, M. K. Sunkara and J. M. Spurgeon, *Energy Environ. Sci.*, 2017, **10**, 2432–2440.
32 Y. Pi, Q. Shao, P. Wang, J. Guo and X. Huang, *Adv. Funct. Mater.*, 2017, **27**, 1700886.
33 O. Kasian, J. P. Grote, S. Geiger, S. Cherevko and K. J. J. Mayrhofer, *Angew Chem. Int. Ed. Engl.*, 2018, **57**, 2488–2491.
34 S. Fierro, T. Nagel, H. Baltruschat and C. Comninellis, *Electrochem. Commun.*, 2007, **9**, 1969–1974.
35 O. Kasian, S. Geiger, T. Li, J.-P. Grote, K. Schweinar, S. Zhang, C. Scheu, D. Raabe, S. Cherevko, B. Gault and K. J. J. Mayrhofer, *Energy Environ. Sci.*, 2019, **12**, 3548–3555.
36 A. Zagalskaya and V. Alexandrov, *ACS Catal.*, 2020, **10**, 3650–3657.
37 L. Fu, P. Cai, G. Cheng and W. Luo, *Sustainable Energy Fuels*, 2017, **1**, 1199–1203.
38 J. J. Velasco-Velez, E. A. Carbonio, C. H. Chuang, C. J. Hsu, J. F. Lee, R. Arrigo, M. Havecker, R. Wang, M. Plodinec, F. R. Wang, A. Centeno, A. Zurutuza, L. J. Falling, R. V. Mom, S. Hofmann, R. Schlogl, A. Knop-Gericke and T. E. Jones, *J. Am. Chem. Soc.*, 2021, **143**, 12524–12534.
39 J. Ruiz Esquius, D. J. Morgan, G. Algara Siller, D. Gianolio, M. Aramini, L. Lahn, O. Kasian, S. A. Kondrat, R. Schlogl, G. J. Hutchings, R. Arrigo and S. J. Freakley, *J. Am. Chem. Soc.*, 2023, **145**, 6398–6409.
40 J. A. Arminio-Ravelo, A. W. Jensen, K. D. Jensen, J. Quinson and M. Escudero-Escribano, *ChemPhysChem*, 2019, **20**, 2956–2963.
41 M. Pourbaix, *Atlas of Electrochemical Equilibria in Aqueous Solutions*, National Association of Corrosion Engineers, 1974.
42 C. He, C. Ma, J. Xia, H. Zhang, S. Han, Y. Tian, A. L. Wang, X. Meng, W. Cao and Q. Lu, *Adv. Funct. Mater.*, 2024, **34**, 2311683.

43 I. C. Man, H. Y. Su, F. Calle-Vallejo, H. A. Hansen, J. I. Martínez, N. G. Inoglu, J. Kitchin, T. F. Jaramillo, J. K. Nørskov and J. Rossmeisl, *ChemCatChem*, 2011, **3**, 1159–1165.

44 A. Grimaud, O. Diaz-Morales, B. Han, W. T. Hong, Y. L. Lee, L. Giordano, K. A. Stoerzinger, M. T. M. Koper and Y. Shao-Horn, *Nat. Chem.*, 2017, **9**, 457–465.

45 D. B. Trimarco, S. B. Scott, A. H. Thilsted, J. Y. Pan, T. Pedersen, O. Hansen, I. Chorkendorff and P. C. K. Vesborg, *Electrochim. Acta*, 2018, **268**, 520–530.

46 S. B. Scott, J. Kibsgaard, P. C. K. Vesborg and I. Chorkendorff, *Electrochim. Acta*, 2021, **374**.

47 M. Hüppauff and B. Lengeler, *J. Electrochem. Soc.*, 1993, **140**, 598.

48 R. K. Pittkowski, S. Punke, A. S. Anker, A. Bornet, N. P. L. Magnard, N. Schlegel, L. G. Graversen, J. Quinson, A. Dworzak, M. Oezaslan, J. J. K. Kirkensgaard, M. Mirolo, J. Drnec, M. Arenz and K. M. O. Jensen, *J. Am. Chem. Soc.*, 2024, **146**, 27517–27527.

49 H. Guo, Z. Fang, H. Li, D. Fernandez, G. Henkelman, S. M. Humphrey and G. Yu, *ACS Nano*, 2019, **13**, 13225–13234.

50 H. Luo, F. Lin, Q. Zhang, D. Wang, K. Wang, L. Gu, M. Luo, F. Lv and S. Guo, *J. Am. Chem. Soc.*, 2024, **146**, 19327–19336.

51 Y. Chen, H. Li, J. Wang, Y. Du, S. Xi, Y. Sun, M. Sherburne, J. W. Ager 3rd, A. C. Fisher and Z. J. Xu, *Nat. Commun.*, 2019, **10**, 572.

52 Q. Dang, H. Lin, Z. Fan, L. Ma, Q. Shao, Y. Ji, F. Zheng, S. Geng, S. Z. Yang, N. Kong, W. Zhu, Y. Li, F. Liao, X. Huang and M. Shao, *Nat. Commun.*, 2021, **12**, 6007.

53 J. Gao, C. Q. Xu, S. F. Hung, W. Liu, W. Cai, Z. Zeng, C. Jia, H. M. Chen, H. Xiao, J. Li, Y. Huang and B. Liu, *J. Am. Chem. Soc.*, 2019, **141**, 3014–3023.

54 Y. Pi, Y. Xu, L. Li, T. Sun, B. Huang, L. Bu, Y. Ma, Z. Hu, C. W. Pao and X. Huang, *Adv. Funct. Mater.*, 2020, **30**, 2004375.

55 L. Zu, X. Qian, S. Zhao, Q. Liang, Y. E. Chen, M. Liu, B. J. Su, K. H. Wu, L. Qu, L. Duan, H. Zhan, J. Y. Zhang, C. Li, W. Li, J. Y. Juang, J. Zhu, D. Li, A. Yu and D. Zhao, *J. Am. Chem. Soc.*, 2022, **144**, 2208–2217.

56 G. Wu, X. Zheng, P. Cui, H. Jiang, X. Wang, Y. Qu, W. Chen, Y. Lin, H. Li, X. Han, Y. Hu, P. Liu, Q. Zhang, J. Ge, Y. Yao, R. Sun, Y. Wu, L. Gu, X. Hong and Y. Li, *Nat. Commun.*, 2019, **10**, 4855.

57 J. A. Gauthier, C. F. Dickens, L. D. Chen, A. D. Doyle and J. K. Nørskov, *J. Phys. Chem. C*, 2017, **121**, 11455–11463.

58 D. A. Kuznetsov, B. Han, Y. Yu, R. R. Rao, J. Hwang, Y. Roman-Leshkov and Y. Shao-Horn, *Joule*, 2018, **2**, 225–244.